Computational Mechanics
https://doi.org/10.1007/s00466-025-02665-7

ORIGINAL PAPER

Virtual element method with non-matching and adaptive meshes for phase field fracture

Bing-Bing Xu[1] · Fan Peng[2] · Philipp Junker[1] · Peter Wriggers[1]

Received: 5 March 2025 / Accepted: 22 June 2025

Abstract
This work presents a stabilization-free virtual element method (VEM) for phase field fracture. The distinctive feature of the virtual element method is its ability to utilize elements of general shape. However, the existence of additional stabilization term in the traditional virtual element method has some drawbacks when solving complex phase field fracture models. Different from the conventional virtual element method, the approach employed in this work eliminates the need for additional stabilization terms, making it more suitable for the phase field modeling of fracture. In this work, the anisotropic phase field fracture model is considered. In order to improve the calculation efficiency, the non-matching mesh ability of VEM and adaptive technique are employed. Since the virtual element method is automatically applicable to elements with general shape, it is easy to handle an arbitrary number of nodes and thus also hanging nodes resulting from the non-matching meshes used to adapt the meshes. Several representative benchmarks show the accuracy and efficiency of the proposed method.

Keywords Virtual element method · Stabilization free · Non-matching mesh · Adaptive technique

1 Introduction

Numerical simulation of fracture is of great importance for engineering applications and material science. In recent years, numerical simulation techniques for predicting fracture problems have mainly been categorized into two approaches: discontinuous and continuous methods [1]. In the discontinuous approach, the crack and its propagation are characterized at the geometric level, which results in discontinuities in the displacements over the crack face. Typical discontinuous methods includes the generalized finite element method (GFEM) [2], the extended finite element method (XFEM) [3], and a special variant of VEM [4]. Although these methods are efficient and flexible, addressing complex crack patterns, such as initiation, branching, and merging, continues to be a significant challenge for discrete approaches. In contrast, continuous approachs (or smeared approachs) do not introduce any discontinuities, as they rely on material degradation modeled through damage mechanics. This approach is able to capture complex crack patterns in a variety of problems in solid mechanics. Typical continuous approachs include gradient damage models [5, 6] and phase field models [7–9].

Phase field modelling of fracture was proposed by Francfort and Marigo [10] based on the Griffith's energetic theory of brittle fracture. By introducing an additional continuous phase field variable $d \in (0, 1]$, the phase field model can be constructed based on a variational formulation including fracture energy. Mathematical principles and applications of phase-field fracture can be found in [7, 11]. For recent work, Chen et al. [12] developed a high-accuracy phase field model that can accurately reproduce arbitrary cohesive laws. Furthermore, Feng and Hai [13] proposed a unified directional energy decomposition method to

✉ Bing-Bing Xu
bingbing.xu@ikm.uni-hannover.de

Fan Peng
pengfan33@chd.edu.cn

Philipp Junker
junker@ikm.uni-hannover.de

Peter Wriggers
wriggers@ikm.uni-hannover.de

[1] Institute of Continuum Mechanics, Leibniz University Hannover, Hannover 30823, Niedersachsen, Germany

[2] School of Science, Chang'an University, Xi'an 710064, Shaanxi, China

Published online: 15 July 2025

incorporate cohesive laws into the phase field model in a 3-D setting Besides, Zhou et al. [14] developed a trust region-based algorithm that demonstrates 2-3 times higher efficiency than ABAQUS's native algorithm, representing a major advance in computational mechanics.

In fact, all the above related works are calculated based on the finite element method. The finite element method is an effective tool for solving phase field modelling of fracture [11, 15–17]. When using the finite element method to solve phase field fracture problems, it is necessary to use a very fine mesh to accurately capture the crack path. In addition, the non-convexity of the potential energy function results in a substantial increase in computational effort. To reduce the total degrees of freedom, a pre-refined mesh can be employed if the crack path is approximately known a priori. A straightforward strategy is to employ a refinement based on a non-matching mesh, enabling localized mesh refinement [18]. Besides, adaptive mesh technology can be used to automatically refine the mesh as the crack propagates [19–21].

Generally, local refinement methods, such as non-matching and adaptive meshing, require numerical methods capable of handling polygonal elements. Polygon elements with hanging nodes can be treated by polygonal finite element method [22] and ariable-node elements [21]. In addition to the most commonly used finite element method, the multi-level hp-FEM and the finite cell method [15] also demonstrate a flexible effect. Additionally, the scaled boundary finite element method (SBFEM) [23] and isogeometric analysis (IGA) [24] offer significant advantages for the application of phase field approaches to fracture.

The virtual element method (VEM) is a new method for arbitrary polygonal elements, which was proposed in [25] and applied to solid mechanics [26, 27]. The basic principle of VEM is to define a projection from the virtual element space to the polynomial space. This projection inevitably leads to rank deficiency in virtual elements, so additional stabilization terms are needed. So far, VEM was applied to solve fracture problems using phase field approaches, see [28–30]. Recent work based on VEM with adaptive mesh for large-strain phase-field fracture can be found in [31]. The flexibility of VEM allows to combine the discrete cutting method with an adaptive phase field model [32]. Beisdes, a high-order VEM has been developed for a fourth-order fracture model [33]. However, for complex phase field models, such as anisotropic phase field fracture model with a spectral decomposition [7], the stabilization term in VEM often lead to poor convergence or even no convergence (if we use the dofi-dofi stabilization).

In order to avoid the influence of the stabilization term, stabilization-free virtual element methods (SFVEM) [34–36] have been constructed. The basic principle is to modify the conventional VEM function space to allow the computation of a higher-order L_2 projection of the gradient. With the appropriate choice of order l [34, 37], the introduction of high-order polynomial space leads to virtual elements with correct rank and results in a more stable VEM, especially for nonlinear problems. For quadrilateral meshes, the simulation results obtained by SFVEM are essentially equivalent to the results obtained by FEM [35, 38]. However, it is inevitable that high-order polynomials used in SFVEM will lead to reduced computational efficiency compared to FEM. Still, SFVEM can be employed for arbitrary shaped elements and yields a consistant treatment of hanging nodes. In this work, the SFVEM is used for the complex phase field fracture model. To enhance computational efficiency, two techniques are employed. The first one involves a rough estimate of the crack path and uses non-matching elements for mesh refinement, ensuring that no new meshes have to be generated during the computation. The second technique is adaptive mesh refinement, in which the mesh is automatically refined when the crack propagates. In order to further improve the computational efficiency, FEM can be used for the quadrilateral elements and SFVEM can be employed for elements with polygonal or other shape.

The paper is organized as follows. The continuum mechanics background and the variational format of phase field model of fracture are given in section 2. The stabilization-free virtual element method for phase field fracture is given in section 3. The finite element method for phase field fracture is addressed in section 4. The adaptive refinement technique can be found in section 5. Numerical examples are provided in section 6. The paper will be summaried in section 7 with conclusion and discussion.

2 Theory of phase field models for fracture

2.1 Phase field representation of the crack

In the study of brittle fracture, the phase field method is widely employed to model and analyze fracture behavior. For a linear elastic body $\Omega \subset \mathbb{R}^d$ with surface boundary $\Gamma = \partial\Omega$ and internal crack surface Γ_s, the crack face can be represented by the regularized crack surface function which is given by the phase field $\phi(\boldsymbol{x})$.

In a quasi-static loading regime, the total potential energy Ψ is the sum of the deformation energy and the crack surface energy Ψ_c

$$\Psi(\boldsymbol{u}, \Gamma_s) = \Psi_b + \Psi_c - \Psi_{ext}, \tag{1}$$

where

$$\Psi_b := \int_\Omega \psi_e(\boldsymbol{\varepsilon}(\boldsymbol{u}), \phi)\mathrm{d}\Omega, \tag{2}$$

$$\Psi_c := \int_{\Gamma_c} \mathcal{G}\mathrm{d}\Gamma, \tag{3}$$

$$\Psi_{ext} := \int_\Omega \boldsymbol{f}\cdot\boldsymbol{u}\mathrm{d}\Omega + \int_{\Gamma_n} \boldsymbol{t}_n\cdot\boldsymbol{u}\mathrm{d}\Gamma. \tag{4}$$

Ψ_b represents the elastic strain energy, ψ_e is the strain energy density functional expressed in terms of strain tensor $\boldsymbol{\varepsilon}(\boldsymbol{u}) = \frac{1}{2}\left(\nabla\boldsymbol{u} + \nabla\boldsymbol{u}^T\right)$ with the displacement field $\boldsymbol{u}$. Besides, Ψ_c represents the material fracture energy and $\mathcal{G}$ is the critical energy release rate. In the expression of the external force potential energy Ψ_{ext}, $\boldsymbol{f}$ is the body force and $\boldsymbol{t}_n$ is the prescribed boundary traction.

In order to avoid discontinuites in traditional fracture problems, the crack surface is regularized by the continuous phase field variable $\phi(\boldsymbol{x}) \in [0, 1]$(as shown in Fig. 1b). Then, the crack surface energy Ψ_c can be approximated as a domain integral, see e.g. [7]

$$\int_{\Gamma_c} \mathcal{G}\mathrm{d}\Gamma \approx \int_\Omega \mathcal{G}\Gamma_{l_0}(\phi)\mathrm{d}\Omega, \tag{5}$$

with

$$\Gamma_{l_0}(\phi) = \frac{\phi^2}{2l_0} + \frac{l_0}{2}|\nabla\phi|^2, \tag{6}$$

where l_0 is the characteristic length scale.

2.2 Energy decomposition

For an isotropic elastic body, the strain energy density can be defined as

$$\psi_e = \frac{1}{2}\lambda\left(\mathrm{tr}\boldsymbol{\varepsilon}\right)^2 + \mu\,\mathrm{tr}\left[(\boldsymbol{\varepsilon})^2\right], \tag{7}$$

where $\mathrm{tr}(\cdot)$ denotes the trace of the tensor, λ and μ are the Lame parameters

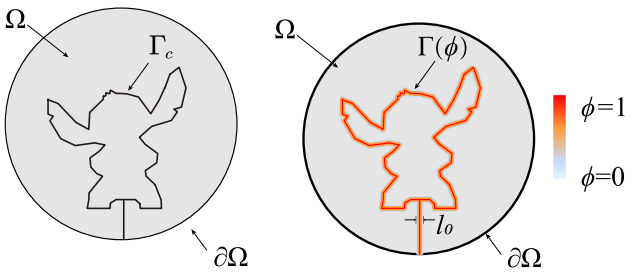

Fig. 1 Body with an internal crack: **a** sharp crack; **b** diffusive crack

$$\lambda = \frac{\nu E}{(1+\nu)(1-2\nu)}, \quad \mu = \frac{E}{2(1+\nu)}, \tag{8}$$

where E is the Young's modulus and ν is the Poisson's ratio. To prevent cracking in the compression region, the strain energy density should be split into positive and negative parts

$$\psi_e(\boldsymbol{\varepsilon}) = g(\phi)\psi_e^+(\boldsymbol{\varepsilon}) + \psi_e^-(\boldsymbol{\varepsilon}). \tag{9}$$

Furthermore, a degradation function $g(\phi)$ is introduced for the tension part. Here, $\psi_e^+(\boldsymbol{\varepsilon})$ and $\psi_e^-(\boldsymbol{\varepsilon})$ are the strain energies obtained by the spectral decomposition of the strain tensor with the form provided in [8]

$$\psi_e^\pm(\boldsymbol{\varepsilon}) = \frac{\lambda}{2}\langle\mathrm{tr}(\boldsymbol{\varepsilon})\rangle^2 + \mu\mathrm{tr}\left[(\boldsymbol{\varepsilon}_\pm)^2\right], \tag{10}$$

The strain tensor $\boldsymbol{\varepsilon}$ is split into positive $(\boldsymbol{\varepsilon}_+)$ and negative $(\boldsymbol{\varepsilon}_-)$ part by spectral decomposition

$$\boldsymbol{\varepsilon}_\pm = \sum_{a=1}^{d}\langle\varepsilon_a\rangle_\pm \boldsymbol{n}_a\otimes\boldsymbol{n}_a \tag{11}$$

where $\langle x\rangle_\pm = (x \pm |x|)/2$, d is the dimension, $\boldsymbol{\varepsilon}_+$ and $\boldsymbol{\varepsilon}_-$ represent the tensile and compressive modes of $\boldsymbol{\varepsilon}$, respectively.

Besides, $g(\phi)$ in Eq.(9) is the degradation function

$$g(\phi) = [(1-\phi)^2 + \kappa], \tag{12}$$

where the small parameter κ is added to prevent numerical singularity.

2.3 Governing equations

By referring to the previous equations, the total potential energy can be written as

$$\begin{aligned}\Psi(\boldsymbol{u},\phi) = &\int_\Omega \left\{\left[(1-\phi)^2+\kappa\right]\psi_e^+(\boldsymbol{\varepsilon}) + \psi_e^-(\boldsymbol{\varepsilon})\right\}\mathrm{d}\Omega \\ &+ \int_\Omega \mathcal{G}\left[\frac{\phi^2}{2l_0} + \frac{l_0}{2}|\nabla\phi|^2\right]\mathrm{d}\Omega - \Psi_{\mathrm{ext}}.\end{aligned} \tag{13}$$

According to Hamilton's principle, the variation of Ψ with respect to $\boldsymbol{u}, \phi$ yields the following bilinear form

$$\begin{cases}\mathcal{A}_{\boldsymbol{u}}(\boldsymbol{u},\boldsymbol{v};\phi) = \mathcal{F}_{\boldsymbol{u}}(\boldsymbol{v}), \\ \mathcal{A}_{\phi 1}(\phi,c;\mathcal{H}_t) + \mathcal{A}_{\phi 2}(\phi,c) + \mathcal{A}_{\phi 3}(\phi,c) = \mathcal{F}_\phi(c),\end{cases} \tag{14}$$

where

$$\boldsymbol{\mathcal{A}}_{\boldsymbol{u}}(\boldsymbol{u},\boldsymbol{v};\phi)=\int_{\Omega}\boldsymbol{\sigma}(\boldsymbol{u};\phi):\boldsymbol{\varepsilon}(\boldsymbol{v})\mathrm{d}\Omega, \tag{15}$$

$$\boldsymbol{\mathcal{F}}_{\boldsymbol{u}}(\boldsymbol{v})=\int_{\Omega}\boldsymbol{f}\cdot\boldsymbol{v}\mathrm{d}\Omega+\int_{\Gamma_N}\boldsymbol{t}_n\cdot\boldsymbol{v}\mathrm{d}\Gamma, \tag{16}$$

$$\mathcal{A}_{\phi 1}(\phi,c;\mathcal{H}_t)=\int_{\Omega}2c\mathcal{H}_t\phi\mathrm{d}\Omega, \tag{17}$$

$$\mathcal{A}_{\phi 2}(\phi,c)=\int_{\Omega}\frac{\mathcal{G}}{l_0}c\phi\mathrm{d}\Omega, \tag{18}$$

$$\mathcal{A}_{\phi 3}(\phi,c)=\int_{\Omega}\mathcal{G}l_0\nabla\phi\cdot\nabla c\mathrm{d}\Omega, \tag{19}$$

$$\mathcal{F}_{\phi}(c)=2c\mathcal{H}_t\mathrm{d}\Omega, \tag{20}$$

where the anisotropic history variable $\mathcal{H}_t=\max_{t\in(0,T]}\psi_e^+$ has to be introduced for the irreversibility of crack growth.

In the above equations, the stress tensor follows from the derivative of strain energy with respect to the strain tensor

$$\boldsymbol{\sigma}=\frac{\partial\psi_e(\boldsymbol{\varepsilon})}{\partial\boldsymbol{\varepsilon}}=\left[(1-\phi)^2+\kappa\right]\frac{\partial\psi_e^+(\boldsymbol{\varepsilon})}{\partial\boldsymbol{\varepsilon}}+\frac{\partial\psi_e^-(\boldsymbol{\varepsilon})}{\partial\boldsymbol{\varepsilon}}. \tag{21}$$

By utilizing Eq.(10), the stress tensor can be obtained in a more complete form as

$$\begin{aligned}\boldsymbol{\sigma}=&\left[(1-\phi)^2+\kappa\right]\left(\frac{1}{2}\lambda\frac{\partial\langle\mathrm{tr}(\boldsymbol{\varepsilon})\rangle_+^2}{\partial\boldsymbol{\varepsilon}}+\mu\frac{\partial(\boldsymbol{\varepsilon}_+:\boldsymbol{\varepsilon}_+)}{\partial\boldsymbol{\varepsilon}}\right)\\&+\frac{1}{2}\lambda\frac{\partial\langle\mathrm{tr}(\boldsymbol{\varepsilon})\rangle_-^2}{\partial\boldsymbol{\varepsilon}}+\mu\frac{\partial(\boldsymbol{\varepsilon}_-:\boldsymbol{\varepsilon}_-)}{\partial\boldsymbol{\varepsilon}}.\end{aligned} \tag{22}$$

According to the chain rule, we have

$$\begin{aligned}\frac{\partial\langle\mathrm{tr}(\boldsymbol{\varepsilon})\rangle_\pm^2}{\partial\boldsymbol{\varepsilon}}&=\frac{\partial\langle\mathrm{tr}(\boldsymbol{\varepsilon})\rangle_\pm^2}{\partial\langle\mathrm{tr}(\boldsymbol{\varepsilon})\rangle_\pm}\frac{\partial\langle\mathrm{tr}(\boldsymbol{\varepsilon})\rangle_\pm}{\partial\mathrm{tr}(\boldsymbol{\varepsilon})}:\frac{\partial\mathrm{tr}(\boldsymbol{\varepsilon})}{\partial\boldsymbol{\varepsilon}}\\&=2\langle\mathrm{tr}(\boldsymbol{\varepsilon})\rangle_\pm H(\pm\langle\mathrm{tr}(\boldsymbol{\varepsilon})\rangle_\pm)\boldsymbol{I},\end{aligned} \tag{23}$$

$$\frac{\partial\mathrm{tr}\left(\boldsymbol{\varepsilon}_\pm^2\right)}{\partial\boldsymbol{\varepsilon}}=\frac{\partial\mathrm{tr}\left(\boldsymbol{\varepsilon}_\pm^2\right)}{\partial\boldsymbol{\varepsilon}^\pm}:\frac{\partial\boldsymbol{\varepsilon}_\pm}{\partial\boldsymbol{\varepsilon}}=2\boldsymbol{\varepsilon}_\pm:\frac{\partial\boldsymbol{\varepsilon}_\pm}{\partial\boldsymbol{\varepsilon}}, \tag{24}$$

where H stands for the Heaviside function. With these results the stress tensor can be expressed by

$$\begin{aligned}\boldsymbol{\sigma}=&[(1-\phi)^2+\kappa]\left[\lambda\langle\mathrm{tr}(\boldsymbol{\varepsilon})\rangle_+H(\langle\mathrm{tr}(\boldsymbol{\varepsilon})\rangle_+)\boldsymbol{I}+2\mu\boldsymbol{\varepsilon}_+:\frac{\partial\boldsymbol{\varepsilon}_+}{\partial\boldsymbol{\varepsilon}}\right]\\&+\lambda\langle\mathrm{tr}(\boldsymbol{\varepsilon})\rangle_-H(-\langle\mathrm{tr}(\boldsymbol{\varepsilon})\rangle_-)\boldsymbol{I}+2\mu\boldsymbol{\varepsilon}_-:\frac{\partial\boldsymbol{\varepsilon}_-}{\partial\boldsymbol{\varepsilon}}.\end{aligned} \tag{25}$$

The elastic constitutive tensor follows from the derivative of the stress tensor with respect to the strain tensor

$$\begin{aligned}\boldsymbol{C}=&\frac{\partial\boldsymbol{\sigma}}{\partial\boldsymbol{\varepsilon}}=\left[(1-\phi)^2+\kappa\right]\\&EMPTY\left[\lambda H^2\left(\langle\mathrm{tr}(\boldsymbol{\varepsilon})\rangle_+\right)\boldsymbol{I}\otimes\boldsymbol{I}+2\mu\frac{\partial\boldsymbol{\varepsilon}_+}{\partial\boldsymbol{\varepsilon}}:\frac{\partial\boldsymbol{\varepsilon}_+}{\partial\boldsymbol{\varepsilon}}\right]\\&+\lambda H^2\left(-\langle\mathrm{tr}(\boldsymbol{\varepsilon})\rangle_-\right)\boldsymbol{I}\otimes\boldsymbol{I}+2\mu\frac{\partial\boldsymbol{\varepsilon}_-}{\partial\boldsymbol{\varepsilon}}:\frac{\partial\boldsymbol{\varepsilon}_-}{\partial\boldsymbol{\varepsilon}}\end{aligned} \tag{26}$$

3 Virtual element method for phase field fracture

As described in many works [5, 11], solving the equations (14) is often very time-consuming. One important reason is that, for the above phase field fracture model, a very small length scale l_0 is needed to accurately approximate the crack. To improve computational efficiency, an estimate of the crack path can be made and local mesh refinement can be performed on the designated domain. In addition, adaptive mesh can be used to automatically refine the mesh based on the phase field value. One simple approach to adaptively refine the mesh is based on hanging nodes.

The virtual element method (VEM) is a new numerical technique which can use arbitrarily shaped elements for the geometric discretization. This feature allows the use of non-matching elements for the adaptive refinement during phase field fracture simulations. As mentioned before, the traditional virtual element method requires additional stabilization terms, which refuce the generality of the method and needs adjustement of the stabilization parameters. Thus, a stabilization free formulation of the virtual element method is preferable.

3.1 Function spaces and projection operators

Let $\mathcal{T}_h$ be a non-overlapping partition of Ω with N^E elements, $\mathcal{E}_h$ be the set of edge of $\mathcal{T}_h$. For each element $E\in\mathcal{T}_h$, the element boundary is denoted by ∂E with outer normal by $\boldsymbol{n}_E$. Besides, the symbol N_E^V represents the number of edges of polygon E and h_E is the diameter.

We firstly introduce a projection operator $\Pi_{1,E}^{\nabla}:\mathcal{H}^1\to\mathbb{P}_1$ by

$$\begin{cases}\displaystyle\int_E\nabla\left(\Pi_{1,E}^{\nabla}v-v\right)\cdot\nabla p_1\mathrm{d}\Omega=0,\quad\forall v\in\mathcal{H}^1(E),p_1\in\mathbb{P}_1(E),\\ \displaystyle\frac{1}{N_E^V}\sum_{i=1}^{N_E^V}\left(\Pi_{1,E}^{\nabla}v-v\right)(V_i)=0,\end{cases} \tag{27}$$

where V_i is the ith vertex. We can construct the first order virtual element space $\mathcal{V}_1(E)$ as

$$\mathcal{V}_1(E)=\left\{v\in\mathcal{H}^1(E):\Delta v\in\mathbb{P}_0(E)\text{ in }E,v|_e\in\mathbb{P}_1(e)\right\}. \tag{28}$$

The values at vertices in E are selected as the degrees of freedom $\boldsymbol{\chi}$.

For each polygon element $E \in \mathcal{T}_h$, based on integration by parts and Gaussian divergence theorem, Eq.(27) is further expanded into

$$\int_E \nabla \Pi_{1,E}^{\nabla} v \cdot \nabla p_1 \mathrm{d}\Omega = -\int_E v \cdot \Delta p_1 \mathrm{d}\Omega + \int_{\partial E} v \cdot \frac{\partial p_1}{\partial \boldsymbol{n}} \mathrm{d}\Gamma. \tag{29}$$

For the first-order VEM space, $\Delta p_1 = 0$. In this case, the projection operator $\Pi_{1,E}^{\nabla}$ can be solved based on the degrees of freedom $\boldsymbol{\chi}$ and additional constant in Eq.(27). Then, a discrete bilinear form is constructed on each element E as

$$\begin{aligned} a_h^E\left(v_h, w_h\right) =& a^E\left(\Pi_{1,E}^{\nabla} v_h, \Pi_{1,E}^{\nabla} w_h\right) \\ &+ S^E\left(\left(I - \Pi_{1,E}^{\nabla}\right) v_h, \left(I - \Pi_{1,E}^{\nabla}\right) w_h\right), \\ & v_h, w_h \in \mathcal{V}_1^h \end{aligned} \tag{30}$$

where S^E is a symmetric bilinear form or stabilization term.

There exist many choices for stabilization terms, but they become more complicated for nonlinear problems. For models that use spectral decomposition for both the stress tensor and the constitutive tensor, the selection of the stabilization term is more complicated. Therefore, we will construct the VEM without stabilization terms.

Inspired by Ref. [34], the basic idea of the stabilization-free virtual element method (SFVEM) is to modify the virtual element space to allow the calculation of the higher order L_2 projection for the gradient. We can construct the local enlarged enhancement virtual element space based on the higher order polynomial projection for given $l \in \mathbb{N}$

$$\mathcal{V}_{1,l}(E) := \left\{v \in \mathcal{H}^1, v|_{\partial E} : v|_e \in \mathbb{P}_1(e), \Delta v \in \mathbb{P}_{l+1}(E)\right\}. \tag{31}$$

Let $\Pi_{l,E}^0 \nabla$ be the L_2 projection of the gradient of function in $\mathcal{V}_{1,l}$ to $\left[\mathbb{P}_l(E)\right]^2$ by the orthogonality condition

$$\int_E \boldsymbol{p} \cdot \Pi_{l,E}^0 \nabla v \mathrm{d}\Omega = \int_E \boldsymbol{p} \cdot \nabla v \mathrm{d}\Omega, \quad \boldsymbol{p} \in \left[\mathbb{P}_l(E)\right]^2. \tag{32}$$

Expanding the right side of Eq.(32) yields

$$\int_E \boldsymbol{p} \cdot \nabla v \mathrm{d}\Omega = \int_{\partial E} \boldsymbol{p} \cdot \boldsymbol{n}_E v - \int_E (\mathrm{div}\boldsymbol{p})\, v \mathrm{d}\Omega. \tag{33}$$

The last term in (33) is computable as $\int_E (\mathrm{div}\boldsymbol{p})\, v \mathrm{d}\Omega = \int_E (\mathrm{div}\boldsymbol{p})\, \Pi_{1,E}^{\nabla} v \mathrm{d}\Omega$. Then, the projection $\Pi_{l,E}^0 \nabla$ can be solved. The parameter l should satisfsfy the following condition for the lowest orders case [34, 39]

$$(l+1)(l+2) > N_E^V - 1. \tag{34}$$

Then, a discrete bilinear form without any stabilization term is constructed on each element E as

$$a_h^E\left(v_h, w_h\right) := \left(\Pi_{l,E}^0 \nabla v_h, \Pi_{l,E}^0 \nabla w_h\right). \tag{35}$$

Lastly, we consider the standard scalar L_2 projection from $\mathcal{V}_1(E)$ to $\mathbb{P}_1(E)$, which can be explicitly expressed as

$$\int_E \left(\Pi_{1,E}^0 v - v\right) p_1 \mathrm{d}\Omega = 0. \tag{36}$$

We can check from the definition of $\mathcal{V}_1(E)$ that $\Pi_{1,E}^0 = \Pi_{1,E}^{\nabla}$ holds true in the lowest order case.

3.2 Stabilization-free VEM for phase field fracture

The stabilization-free virtual element method is selected for the variational formulation (see Eq.(14)). Two different projection operators, which are discussed in section 3.1, are employed. For a matrix description, the $\mathcal{H}_1$ projection $\Pi_{1,E}^{\nabla} v_h$ can be expanded in the basis $\mathbb{P}_1(E)$ as

$$\Pi_{1,E}^{\nabla} v_h = \boldsymbol{m}_1^T \boldsymbol{\Pi}_{1,*}^{\nabla} \tilde{\boldsymbol{v}} = \boldsymbol{m}_1^T \boldsymbol{\Pi}_{1,*}^0 \tilde{\boldsymbol{v}}, \tag{37}$$

where $\boldsymbol{m}_1$ is the first order scaled polynomial, $\boldsymbol{\Pi}_{1,*}^{\nabla}$ and $\boldsymbol{\Pi}_{1,*}^0$ are the matrices representation of operator $\Pi_{1,E}^{\nabla}$ and $\Pi_{1,E}^0$ with respect to the basis of $\mathbb{P}_1(E)$, respectively.

For the L_2 projection operator, we can denote $\boldsymbol{\Pi}^m$ as the matrix representation of the operator $\Pi_{l,E}^0 \nabla$ with respect to the basis of $[\mathbb{P}_l(E)]^2$. Then the gradient of the variable v_h can be approximated as

$$\nabla v_h = \Pi_{l,E}^0 \nabla v_h = \left(\boldsymbol{N}^p\right)^T \boldsymbol{\Pi}^m \tilde{\boldsymbol{v}}, \tag{38}$$

where

$$\left(\boldsymbol{N}^p\right)^T := \begin{bmatrix} 1 & \xi & \eta & \cdots & \eta^l & 0 & 0 & 0 & \cdots & 0 \\ 0 & 0 & 0 & \cdots & 0 & 1 & \xi & \eta & \cdots & \eta^l \end{bmatrix} = \begin{bmatrix} \boldsymbol{m}_l^T & & \\ & & \boldsymbol{m}_l^T \end{bmatrix}, \tag{39}$$

and $\boldsymbol{m}_l$ is the basic for the scaled polynomials of order l.

Using the above definition, the projection between $\Pi_{1,*}^{\nabla}\phi$ and ϕ_h can be expressed as

$$\Pi_{1,*}^{\nabla} \phi = \boldsymbol{m}_1^T \boldsymbol{\Pi}_{1,*}^{\nabla} \tilde{\boldsymbol{\phi}}, \tag{40}$$

where $\tilde{\boldsymbol{\phi}}$ is the vector consisting of the values ϕ_h of each node in element E. Besides, the strain $\boldsymbol{\varepsilon}$($\hat{\boldsymbol{\varepsilon}}$ in Voigt notation) can be approximated by

$$\hat{\boldsymbol{\varepsilon}}(\boldsymbol{u}) = \boldsymbol{A}\left[\left(\boldsymbol{N}^p\right)^T \boldsymbol{\Pi}^m \otimes \mathbb{I}_2\right] \tilde{\boldsymbol{u}} = \boldsymbol{A}\left(\boldsymbol{N}_p\right)^T \boldsymbol{\Pi}_m \tilde{\boldsymbol{u}} \tag{41}$$

where $\otimes$ is the Kronecker product and $\mathbb{I}_2$ represents 2×2 order identity matrix, and

$$\boldsymbol{A} = \begin{bmatrix} 1 & 0 & 0 & 0 \\ 0 & 0 & 0 & 1 \\ 0 & 1 & 1 & 0 \end{bmatrix}, \boldsymbol{N}_p = \boldsymbol{N}^p \otimes \mathbb{I}_2, \boldsymbol{\Pi}_m = \boldsymbol{\Pi}^m \otimes \mathbb{I}_2. \tag{42}$$

Using the above discretization, the residual for the elastic field $\boldsymbol{R}^{\boldsymbol{u}}$ and the phase field $\boldsymbol{R}^{\phi}$ can be written as

$$\boldsymbol{R}_E^{\boldsymbol{u}} = -\boldsymbol{\Pi}_m^T \int_E \boldsymbol{N}_p \boldsymbol{A}^T \hat{\boldsymbol{\sigma}} \mathrm{d}\Omega, \tag{43}$$

$$\begin{aligned} \boldsymbol{R}_E^{\phi} = &- \left(\boldsymbol{\Pi}^m\right)^T \int_E \mathcal{G} l_0 \boldsymbol{N}^p \nabla \phi \mathrm{d}\Omega - \left(\boldsymbol{\Pi}_{1,*}^0\right)^T \int_E \frac{\mathcal{G}}{l_0} \boldsymbol{m}_1 \phi \mathrm{d}\Omega \\ &+ \left(\boldsymbol{\Pi}_{1,*}^0\right)^T \int_E 2(1-\phi) \boldsymbol{m}_1 \mathcal{H}_t \mathrm{d}\Omega. \end{aligned} \tag{44}$$

The stiffness matrix at elemental level can be derived by linearization of Eqs.(43) and (44)

$$\boldsymbol{K}_E^{\boldsymbol{uu}} = -\frac{\partial \boldsymbol{R}_E^{\boldsymbol{u}}}{\partial \tilde{\boldsymbol{u}}} = \boldsymbol{\Pi}_m^T \int_E \boldsymbol{N}_p \boldsymbol{A}^T \hat{\boldsymbol{C}} \boldsymbol{A} \boldsymbol{N}_p^T \mathrm{d}\Omega \boldsymbol{\Pi}_m, \tag{45}$$

$$\begin{aligned} \boldsymbol{K}_E^{\phi\phi} = -\frac{\partial \boldsymbol{R}_E^{\phi}}{\partial \tilde{\boldsymbol{\phi}}} = &\left(\boldsymbol{\Pi}_{1,*}^0\right)^T \int_E \boldsymbol{m}_1 \left(2\mathcal{H}_t + \frac{\mathcal{G}}{l_0}\right) \boldsymbol{m}_1^T \mathrm{d}\Omega \boldsymbol{\Pi}_{1,*}^0 \\ &+ \left(\boldsymbol{\Pi}^m\right)^T \int_E \mathcal{G} l_0 \boldsymbol{N}^p \left(\boldsymbol{N}^p\right)^T \mathrm{d}\Omega \boldsymbol{\Pi}^m \end{aligned} \tag{46}$$

In this work, the staggered scheme is selected for the hybrid model

$$\tilde{\boldsymbol{\phi}}_{t+\Delta t} = \tilde{\boldsymbol{\phi}}_t + \left(\boldsymbol{K}^{\phi\phi}\right)^{-1} \boldsymbol{R}^{\phi}, \tag{47}$$

$$\tilde{\boldsymbol{u}}_{t+\Delta t} = \tilde{\boldsymbol{u}}_t + \left(\boldsymbol{K}^{\boldsymbol{uu}}\right)^{-1} \boldsymbol{R}^{\boldsymbol{u}}. \tag{48}$$

Integrations in Eqs.(43) to (46) are performed by dividing element E into triangles. In fact, the kernel function of the above integral only includes polynomials and their products, so the integral can be shifted to the element boundary ∂E for calculation by using the divergence theorem:

$$\int_E \xi^p \eta^q \mathrm{d}\Omega = \frac{1}{2} \int_{\partial E} \left[\frac{\xi^{p+1} \eta^q}{p+1} n_x + \frac{\xi^p \eta^{q+1}}{q+1} n_y \right] \mathrm{d}\Gamma, \tag{49}$$

where $\boldsymbol{n} = (n_x, n_y)$ is the outward normal.

For the stabilization-free virtual element method, the discretization format, analysis process and calculation accuracy are very similar to traditional finite element method. Therefore, SFVEM is a very advantageous technique for dealing with non-matching meshes and adaptive refinements.

4 Finite element method for phase field fracture

Within the finite element method, the solution domain Ω is discretized by using a mesh family $\{\mathcal{T}_h\}$. The bacis function of function element space is known and the variables can be approximated by the standard first-order FEM shape function

$$\boldsymbol{u} = \sum_{I=1}^{n} N_{\boldsymbol{u}I}^E(\boldsymbol{x}) \boldsymbol{u}_I^E = \boldsymbol{N} \tilde{\boldsymbol{u}}, \phi = \sum_{I=1}^{n} N_{\phi I}^E(\boldsymbol{x}) \phi_I^E = \boldsymbol{N} \tilde{\boldsymbol{\phi}}. \tag{50}$$

Then, the residual for the elastic field $\boldsymbol{R}^{\boldsymbol{u}}$ and the phase field $\boldsymbol{R}^{\phi}$ can be written as

$$\boldsymbol{R}_E^{\boldsymbol{u}} = -\int_E \boldsymbol{B}_{\boldsymbol{u}}^T \hat{\boldsymbol{\sigma}} \mathrm{d}\Omega, \tag{51}$$

$$\begin{aligned} \boldsymbol{R}_E^{\phi} = &- \int_E \mathcal{G} l_0 \boldsymbol{B}_{\phi}^T \nabla \phi \mathrm{d}\Omega - \int_E \frac{\mathcal{G}}{l_0} \boldsymbol{N}^T \phi \mathrm{d}\Omega \\ &+ \int_E 2(1-\phi) \boldsymbol{N}^T \mathcal{H}_t \mathrm{d}\Omega, \end{aligned} \tag{52}$$

where $\boldsymbol{B}_{\boldsymbol{u}}$ and $\boldsymbol{B}_{\phi}$ are the spacial derivatives of the shape functions. The stiffness matrix can be obtained for each element by

$$\boldsymbol{K}_E^{\boldsymbol{uu}} = -\frac{\partial \boldsymbol{R}_E^{\boldsymbol{u}}}{\partial \tilde{\boldsymbol{u}}} = \int_E \boldsymbol{B}_{\boldsymbol{u}}^T \hat{\boldsymbol{C}} \boldsymbol{B}_{\boldsymbol{u}} \mathrm{d}\Omega, \tag{53}$$

$$\begin{aligned} \boldsymbol{K}_E^{\phi\phi} = -\frac{\partial \boldsymbol{R}_E^{\phi}}{\partial \tilde{\boldsymbol{\phi}}} = &\int_E \mathcal{G} l_0 \boldsymbol{B}_{\phi}^T \boldsymbol{B}^T \mathrm{d}\Omega \\ &+ \int_E \left(\frac{\mathcal{G}}{l_0} + 2\mathcal{H}_t\right) \boldsymbol{N}^T \boldsymbol{N} \mathrm{d}\Omega. \end{aligned} \tag{54}$$

Again, the staggered scheme can be applied for the solution of the model.

There is no doubt that the finite element method offers high efficiency and precision in solving the given phase field model. However, a large number of elements are required to discretize the geometric model prior to calculation, significantly increasing the computational cost.

5 Adaptive refinement strategy and hybrid scheme

When using the phase field method to simulate fracture problems, a very fine mesh is required in the region of the crack to accurately capture the crack propagation process. We can predict the crack path and pre-discretize the model

with fine elements in the specified area. Additionally, adaptive refinement can be used to automatically refine the elements. Among different possibilites to refine a mesh, the hanging-node approach is very simple and especially for virtual element method, see [40, 41]. This is due to the possibility to add additional nodes to a virtual element without destroying the continuity.

5.1 Adaptive refinement

In phase field fracture modeling, the phase field threshold can be selected as a refinement indicator, a scheme commonly employed in previous studies [19, 20, 32]. In this work, the elements are marked for refinement if the phase field values are higher than the threshold ϕ_t

$$\phi_i > \phi_t \tag{55}$$

where ϕ_i is the phase field value in the center of the element. The selection of the threshold ϕ_t will be discussed in the examples.

As shown in Fig. 2, during the phase field iteration process, if the phase field value at the element center satisfies Eq.(55), the element can be devided into different sub-elements and the refined element may undergo further subdivision. The refinement process will stop until the effective element size is h_c, where h_c is the threshold of element size. In the adaptive refinement scheme, the displacement $\boldsymbol{u}$ and phase field variable ϕ should be projected from the coarser mesh to the finermesh, respectively.

5.2 Hybrid scheme

With adaptive technology, the computational domain can initially be divided into larger quadrilateral elements (polygonal elements are also acceptable). During mesh adaptation, polygonal elements and quadrilateral elements with additional nodes are generated as shown in Fig. 2. In fact, the adaptively generated elements only make up a small part of the total quantity of elements. We can use SFVEM only for the newly generated elements and use FEM for the quadrilateral elements, which will improve our computational efficiency.

6 Numerical examples

6.1 Single-edge notched tension test

The first benchmark test considers a square plate containing a horizontal pre-crack as shown in Fig. 3. The size of the square specimen is selected as $L = 0.5$mm. The bottom of the plate is fixed in Y-direction and a vertical displacement u_y is applied on the top. The material parameters are selected as $E = 210$GPa, $\nu = 0.3$, $\mathcal{G} = 2.7 \times 10^{-3}$kN/mm. The regularization parameter is selected as $l_0 = 0.015$ mm, The displacement increment is initially selected as $\Delta u_y = 1 \times 10^{-5}$ mm for the first 500 time steps. After that, the displacement increment is reduced to $\Delta u_y = 1 \times 10^{-6}$ mm.

Firstly, we use a non-matching mesh for the calculation. Since the crack path can be roughly predicted in this problem, a pre-refined mesh can be used as shown in Fig. 3. The element size in the pre-refined domain is $h_{max} = 0.005 < l_0/2$, and the non-matching meshes are used between elements of different sizes. In areas far away from the pre-refined domain, we can use quadrilateral mesh or polygonal mesh for discretization, as shown in Fig. 3. In the case of the quadrilateral mesh, the number of nodes is 3925. Additionally, for the polygonal mesh, the number of nodes is 6249. The finite element method with a fine mesh (the number of nodes is 40501) is chosen for comparison.

The displacement-loading curves using the pre-refined non-matching meshes are computed and given in Fig. 4. The curves are in good agreement with the curve obtained by FEM with a fine mesh. Since a non-matching mesh, see

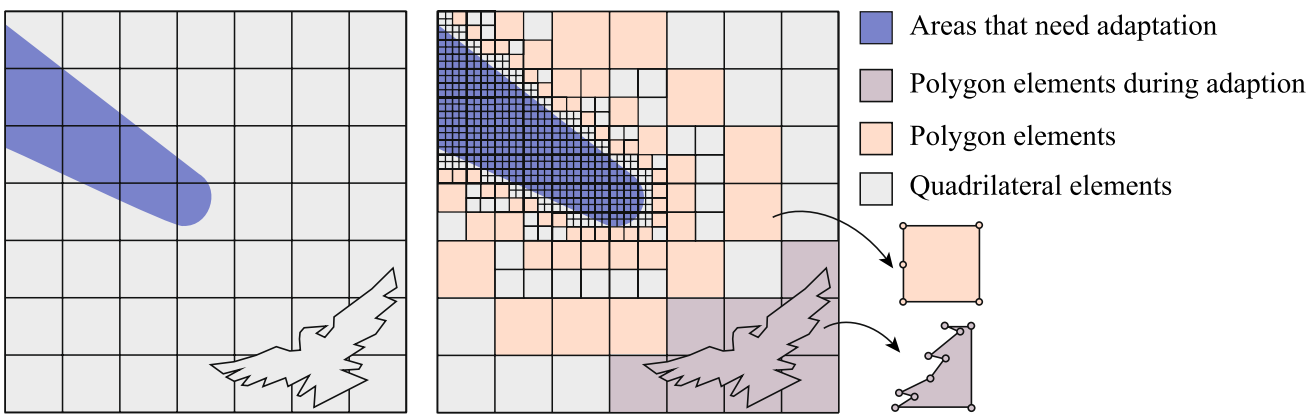

Fig. 2 Adaptive mesh refinement and polygon elements generation

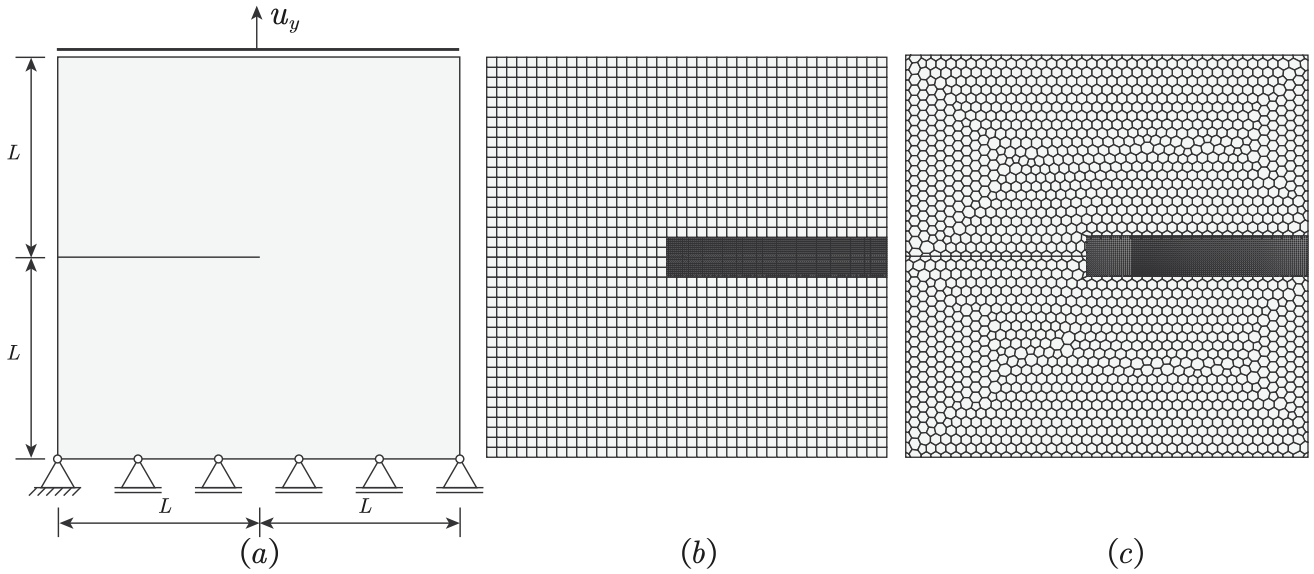

Fig. 3 Single-edge notched tension test, **a** Geometry, loading and boundary conditions; **b** discretization of the specimen by using non-matching meshes (quad mesh); **c** discretization of the specimen by using non-matching meshes (polygon mesh)

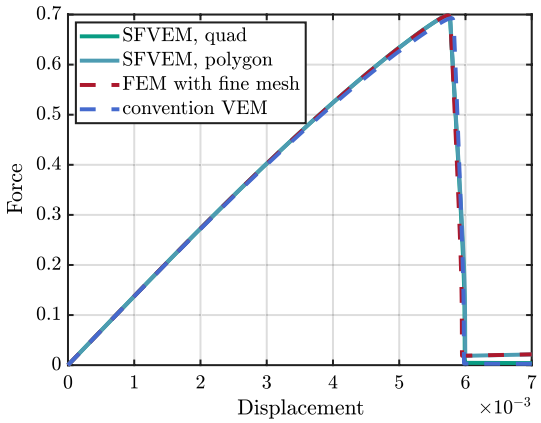

Fig. 4 Force-displacement curves for single edge notched tension test. SFVEM for non-matching meshes

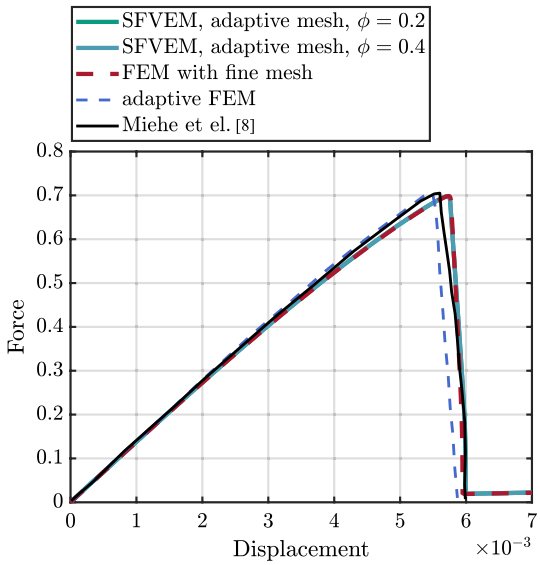

Fig. 5 Force-displacement curves for single edge notched tension test. Adaptive SFVEM with different threshold ϕ_t and reference results

Fig. 3b and c is used, the number of degrees of freedom is low and the computing speed is faster than FEM at the fine mesh. Besides, the SFVEM can discretize the domain in a more flexible manner, even polygonal meshes. We also considered the conventional VEM for the phase-field fracture under the current constitutive assumption. The displacement-loading curve obtained by the conventional VEM is given in Fig. 4. Compared with the conventional VEM, the SFVEM proposed in this work are in better agreement with the FEM results.

The adaptive technique is also used in this example. In this case, the initial element size of the coarse mesh is $h_{max} = 0.0385$ mm. The maximum refinement level is 3 and the sizes of the refined elements are 0.0048125 mm, smaller than $l_0/2$. In this example, the adaptive threshold ϕ_t is selected as $\phi_t = 0.2$ and $\phi_t = 0.4$ for comparison. The displacement-loading curve for the adaptive mesh is obtained, see Fig. 5. The curve is in good aggrement with the curve obtained by FEM with the fine mesh. Very similar results can be observed for different adaptive thresholds ϕ_t. In fact, a larger threshold ϕ_t will further improve the computational efficiency. Besides, the solution from the hybrid adaptive finite element phase-field method [20] is also given for comparison, see Fig 5. The load–displacement curves obtained by SFVEM are in better agreement with the curve obtained in [8].

The calculation times for different meshes and different methods are shown in Table 1. In this work, we use

MATLAB in a notebook with a 2.5 GHz 8-Core Intel Core i9 processor. It can be seen that the use of adaptive mesh can greatly improve the computational efficiency of phase field fracture analysis.

The crack patterns for tensile loading are illustrated at different loading times in Fig. 6. Very similar crack patterns of three meshes at different loading time can be observed.

Table 1 Single edge notched tension test: computational times

Method	Times (s)	
FEM	26062	
SFVEM,adaptive mesh, $\phi_t = 0.2$	2790	10.7%
SFVEM,adaptive mesh, $\phi_t = 0.4$	1300	4.9%

6.2 Single-edge notched pure shear test

In this example, the single edge notched pure shear test is simulated. The geometry and material parameters are the same as in the previous example. A horizontal rightward displacement u_x is applied on the top of the square plate, as shown in Fig. 7. The regularization parameter is selected as $l_0 = 0.015$mm, The displacement increment is initially selected for $\Delta u_x = 1 \times 10^{-5}$ mm for the first 800

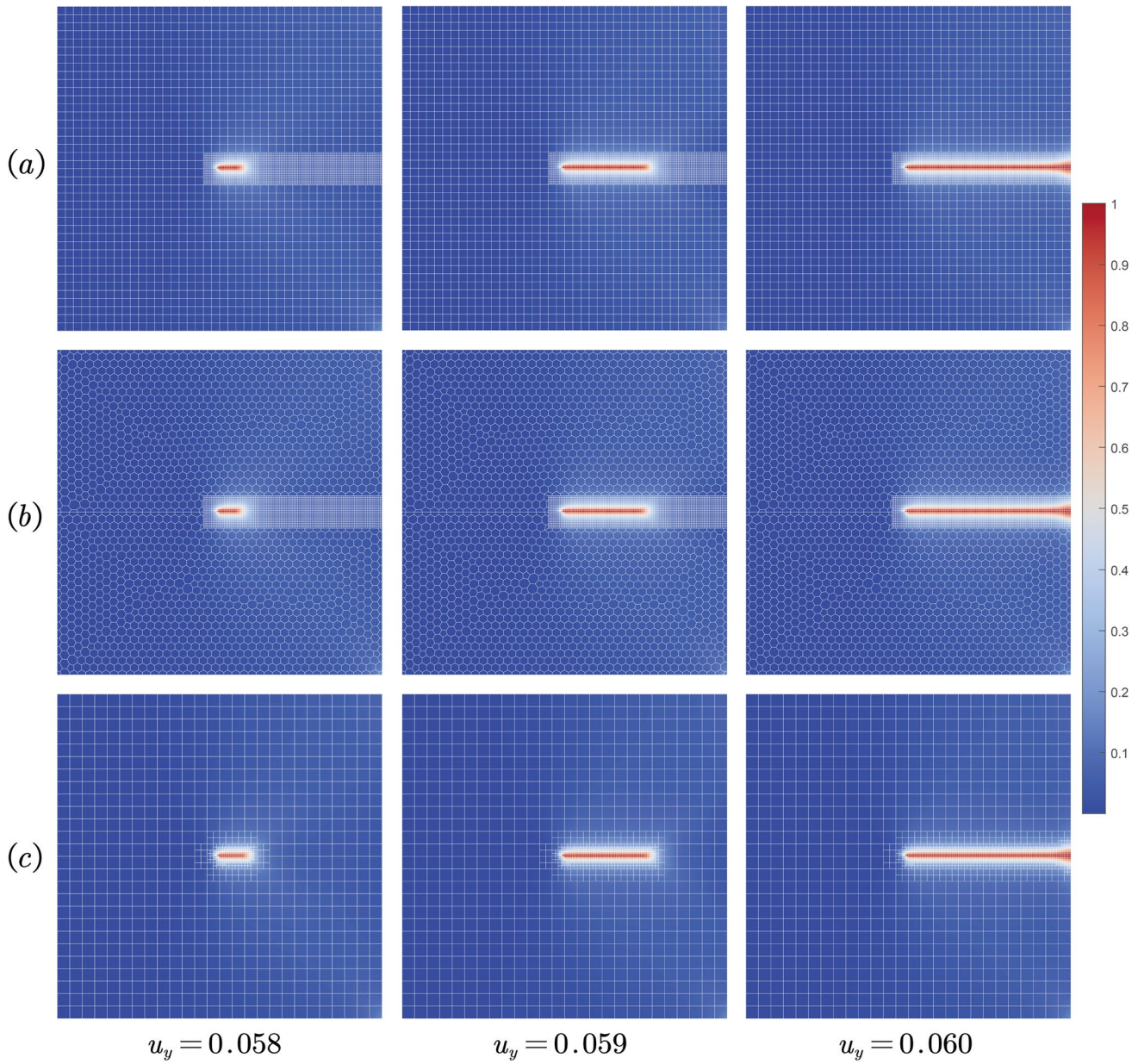

Fig. 6 Crack patterns for single notched plate for different times. **a** SFVEM with non-matching quadrilateral mesh, **b** SFVEM with non-matching polygonal mesh, **c** SFVEM with adaptive mesh

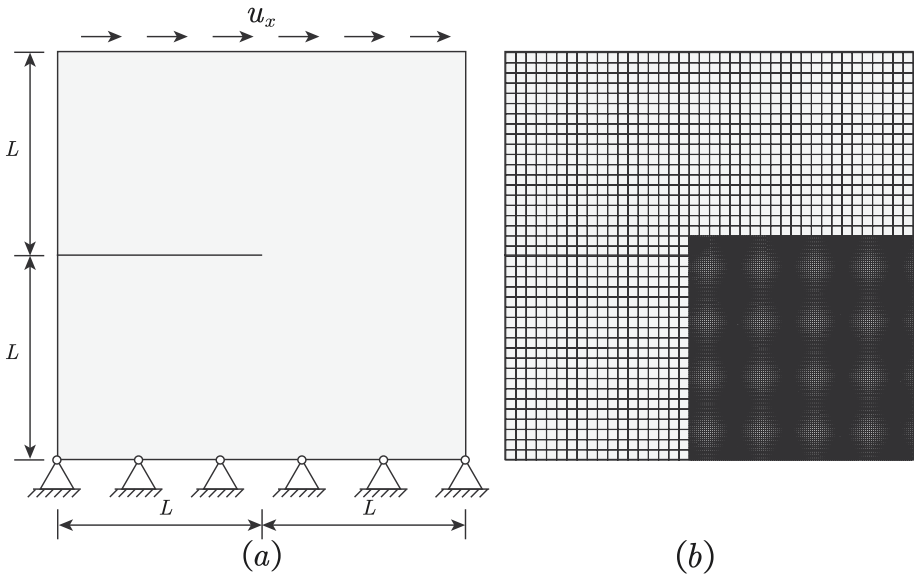

Fig. 7 Single-edge notched pure shear test, **a** Geometry, loading and boundary conditions; **b** discretization of the specimen by using non-matching mesh (quad mesh)

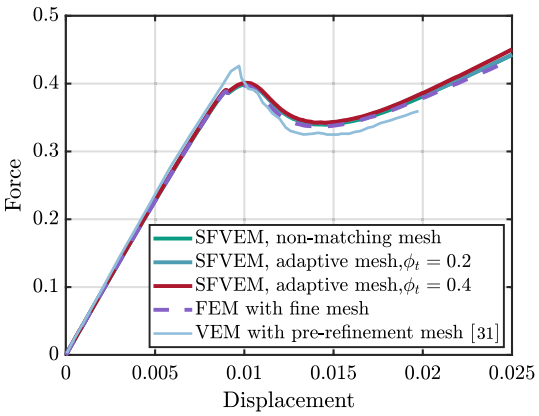

Fig. 8 Load–displacement curve of the single edge notched pure shear test

time steps. Then the displacement increment is reduced to $\Delta u_x = 5 \times 10^{-6}$ mm for the next 3400 time steps.

A non-matching mesh as shown in Fig. 7 is considered as well as the adaptive mesh refinement. The element size of the initial mesh for the adaptive method is $h_{max} = 0.0385$. The maximum refinement level is 3 and the resulting size of the fine elements is 0.0048125, smaller than $l_0/2$. In this example, the adaptive threshold ϕ_t is selected as $\phi_t = 0.2$ and $\phi_t = 0.4$ for comparison.

The displacement-loading curve for the adaptive mesh is obtained, see Fig. 8. The load–displacement curves obtained by non-matching mesh and adaptive mesh are all in good agreement with the curve obtained by FEM with the fine mesh. The computation with the adaptive mesh only takes 20% and 14% of the computation time used for FEM with a fine mesh (the number of nodes is 40501) for $\phi_t = 0.2$ and $\phi_t = 0.4$, respectively. Besides, the load–displacement curve obtained by VEM with local pre-refinement mesh [28] is given for comparison. Easy to find that similar results can be obtained. The crack patterns for different times are given in Fig. 9.

It is worth noting that if the traditional VEM (with stabilization) is used, the convergence rate in this case is significantly slower, and in some instances, no convergent results can be obtained for the current anisotropic phase-field model. Some special stabilization technical in VEM [32] should be introduced to obtain a better convergence. This highlights the advantages of the stabilization-free virtual element method in addressing phase-field fracture problems.

6.3 L-shape panel under mixed-mode failure

The mixed-mode failure test of a L-shape panel was carried out experimentally in [42]. The geometry, loading and boundary conditions of the specimen is given in Fig. 10. The specimen is fixed at the bottom and displacement load is applied upward at a distance of 30 to the right edge. The properties parameters are selected as $E = 25.85$ GPa, $\nu = 0.18$, $\mathcal{G} = 9.5 \times 10^{-5}$ kN/mm. The regularization parameter is chosen as $l_0 = 2$ mm.

During the loading process, the displacement increment in the vertical direction $\Delta u = 2 \times 10^{-3}$ mm for each time step. The mesh adaptive refinement is adopted and the initial geometry is discretized with 1875 coarse elements with element size $h_{max} = 10$ mm. The maximum refinement level is 4, and the resulting size of the fine elements is 0.625 mm, smaller than $l_0/2$. To enhance computational efficiency, the stabilization-free virtual element method is applied to polygonal elements (e.g., elements with hanging nodes), while the finite element method is employed for quadrilateral elements. Besides, the finite element method with very

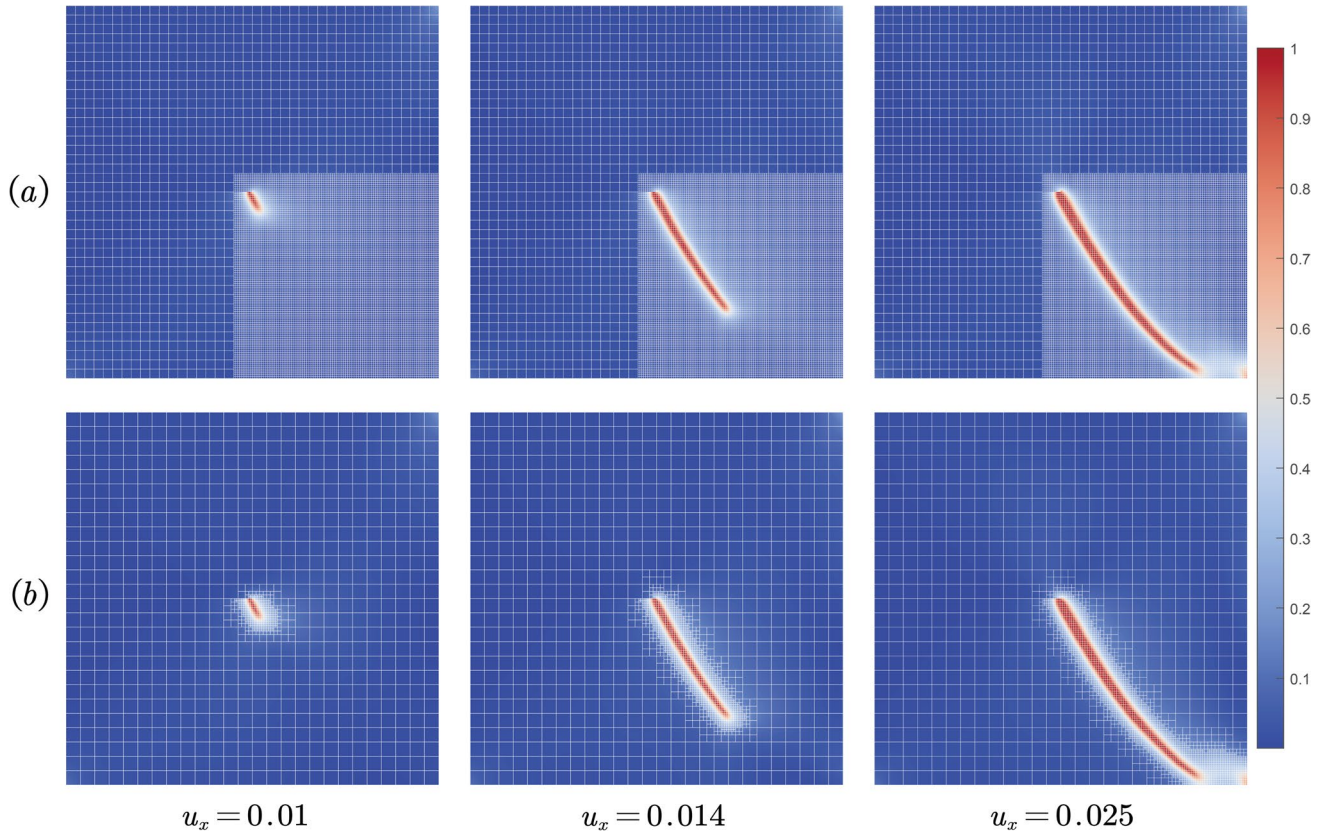

Fig. 9 Crack patterns for single notched plate pure shear test for different times. **a** SFVEM with non-matching mesh, **b** SFVEM with adaptive mesh ($\phi_t = 0.2$)

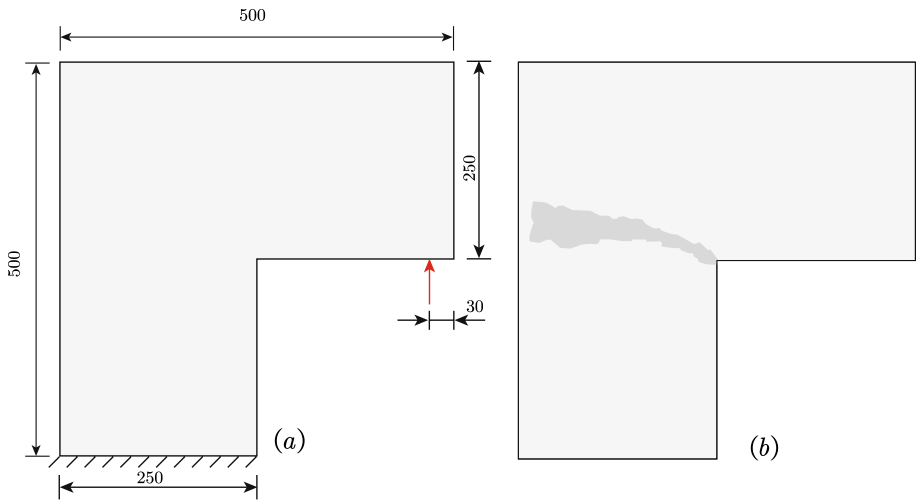

Fig. 10 L-shaped panel, **a** Geometry, loading and boundary conditions; **b** Crack paths

fine mesh (with 58493 elements and 58849 nodes) is used for comparison.

The load–displacement curve is given in Fig. 11. Easy to find that the reaction force agrees very well with the solution obtained by FEM with a fine mesh. Besides, we consider the solution obtained by adaptive finite element method using a volume weighted quickselect algorithm, see [19]. Obviously, the adaptive algorithm combined with the virtual element technology is in good agreement with the classical adaptive finite element method. The crack propagation pattern and corresponding hybrid adaptive meshe are illustrated in Fig. 12. It can be seen that the crack propagation path is in good agreement with the experimental results. In addition, due to the use of adaptive technology, the computational efficiency is greatly improved. Compared with

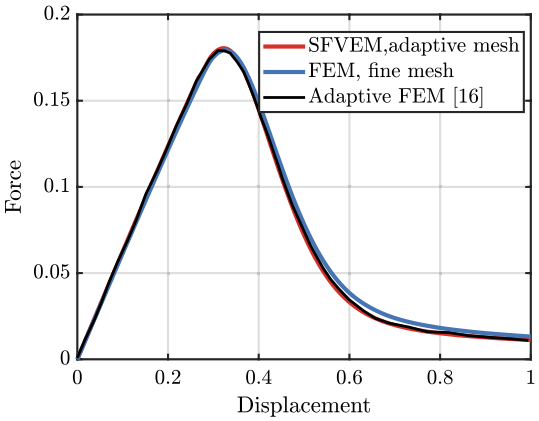

Fig. 11 Load–displacement curve of L-shaped panel test

FEM with fine mesh, the solution time is reduced by nearly 90%.

6.4 Notched plate with hole

A notched plate containing a hole is considered here, with the geometric description and the boundary conditions given in Fig. 13. The specimen is fixed ($u_x = u_y = 0$) at the bottom hole and displacement $u_y = u > 0$ is given at the top hole. The material properties of the specimen is assumed as $E = 6$GPa, $\nu = 0.22(\lambda = 1.94$ GPa and $\nu = 2.45$ GPa). Besides, $\mathcal{G} = 2.28 \times 10^{-3}$ kN/mm, and $l_0 = 0.1$ mm. The initial computational domain consists of 1767 elements and 1892 nodes. The numerical simulations have been performed with fixed displacement increments of $\Delta u = 1 \times 10^{-3}$ mm.

The phase field evolution of the continuously monitored displacement is shown in Fig. 14. It can be seen that as the displacement load increases, the crack expands and the mesh adapts accordingly. Due to the use of the phase field model, a very significant benefit observed is that the second

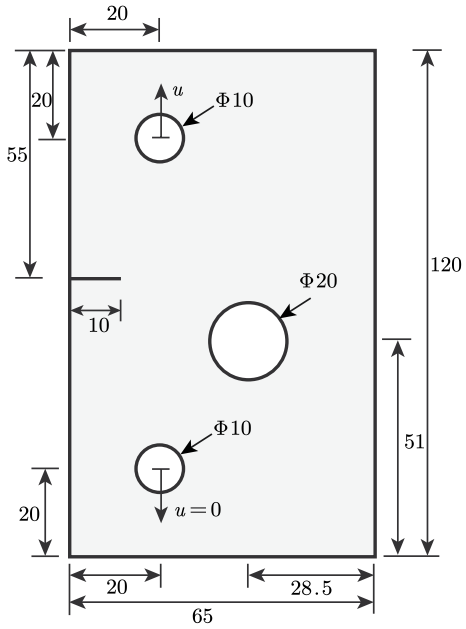

Fig. 13 Notched plate with hole: geometry and boundary conditions

crack path propagates without any initial fracture. Generally, this is not possible using conventional discontinuity methods, such as XFEM. The reaction force curves obtained by STVEM and NURBS-based isogeometric approach [43] are given in 15.

7 Conclusion

In this work, the stabilization-free virtual element method is proposed for the 2D phase field modeling of fracture. Taking the capability of the virtual element method to accommodate polygonal elements, techniques such as pre-refined meshes or adaptive meshing can be employed to enhance

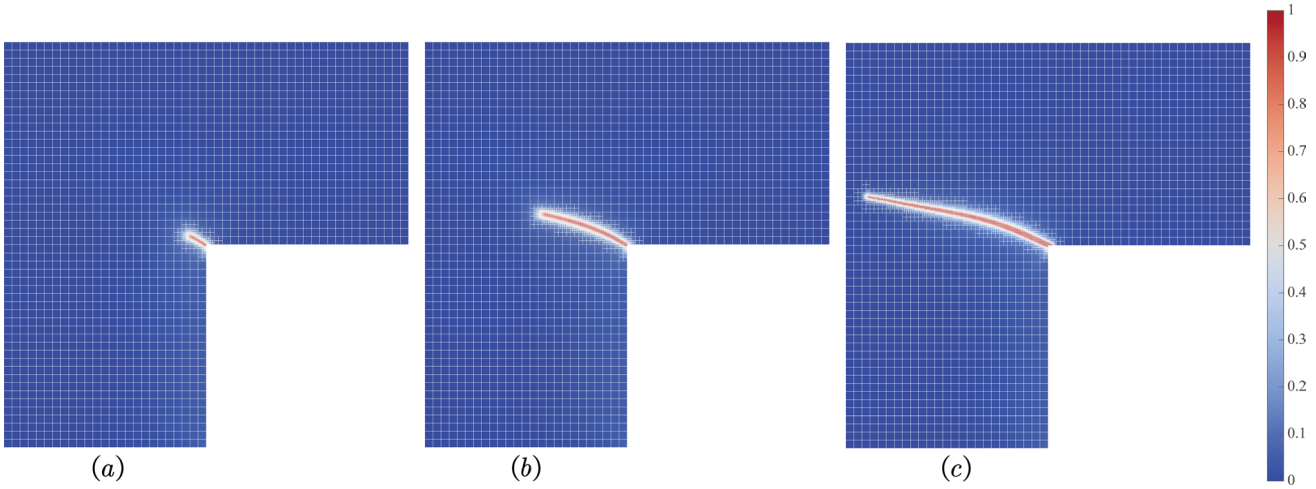

Fig. 12 The crack growth of the L-shaped panel, **a** $u_y = 0.4$, **b** $u_y = 0.50$, **c** $u_y = 1.00$

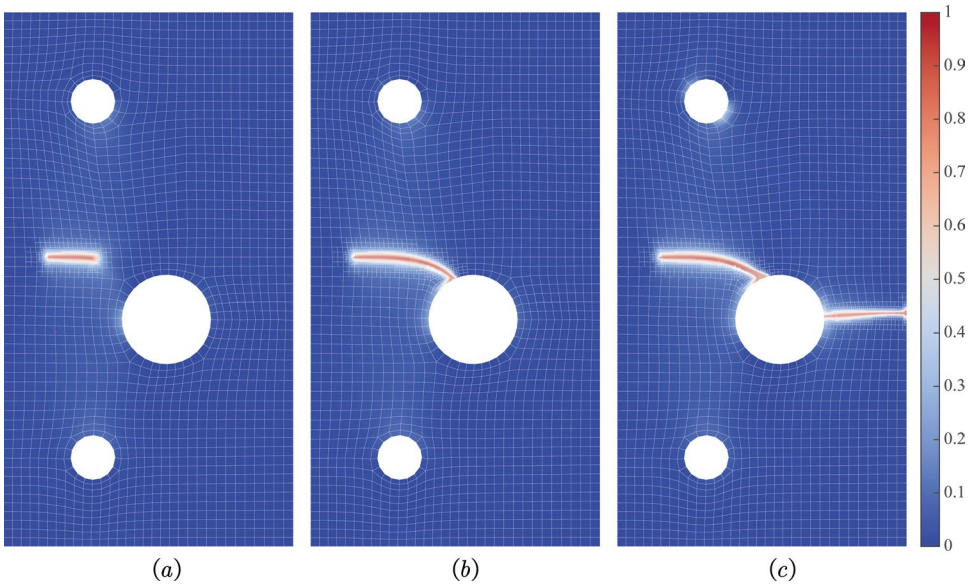

Fig. 14 Phase field and corresponding adaptive meshes of the notched plate with hole test at **a** $u_y = 0.55$ mm, **b** $u_y = 0.7$ mm, **c** $u_y = 1.5$ mm, respectively

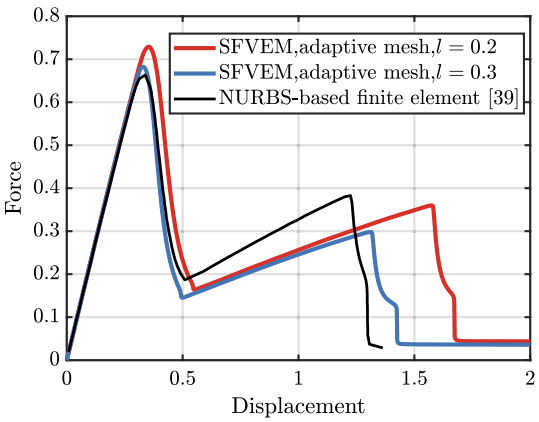

Fig. 15 Reaction force versus displacement curves of the notched plate with hole

the computational efficiency of phase-field fracture problems. Compared with the traditional virtual element method with "dofi" stabilization terms, more stable results can be obtained by the stabilization-free VEM. For the anisotropic model used in this work, the stabilization-free VEM has better convergence, while the traditional VEM with with "dofi" stabilization may not convergence at all. Numerical examples show that the method has a high accuracy and can greatly improve the numerical efficiency. In the future, the above work can be extended to other fracture problems when using the phase field approach.

Acknowledgements The first and last authors are grateful for the support provided by the Alexander von Humboldt Foundation, Germany. The second author is grateful for the support provided by the Natural Science Basic Research Plan in Shaanxi Province, China (Grant No.2025JC-YBQN-022).

Funding Open Access funding enabled and organized by Projekt DEAL.

References

1. Zhuang X, Zhou S, Huynh G, Areias P, Rabczuk T (2022) Phase field modeling and computer implementation: a review. Eng Fracture Mech 262:108234
2. Strouboulis T, Babuska I, Copps K (2000) The design and analysis of the generalized finite element method. Comput Methods Appl Mech Eng 181:43–69
3. Moes N, Dolbow J, Belytschko T (1999) A finite element method for crack growth without remeshing. Int J Numerical Methods Eng 46:131–150
4. Hussein A et al (2019) A computational framework for brittle crack-propagation based on efficient virtual element method. Finite Elements Anal Design 159:15–32
5. Rabczuk T (2013) Computational methods for fracture in brittle and quasi-brittle solids: state-of-the-art review and future perspectives. Int Scholarly Res Notices 2013:849231
6. Peerlings RR, de R Rene Borst, Brekelmans WAM, de Jhp Henk Vree, Spee I, (1996) Some observations on localisation in non-local and gradient damage models. European J Mechanics A-solids 15:937–953
7. Miehe C, Welschinger F, Hofacker M (2010) Thermodynamically consistent phase-field models of fracture: variational principles and multi-field FE implementations. Int J Numerical Methods Eng 83:1273–1311
8. Miehe C, Hofacker M, Welschinger F (2010) A phase field model for rate-independent crack propagation: robust algorithmic

implementation based on operator splits. Comput Methods Appl Mechanics Eng 199:2765–2778
9. Borden MJ, Verhoosel CV, Scott MA, Hughes TJ, Landis CM (2012) A phase-field description of dynamic brittle fracture. Comput Methods Appl Mechanics Eng 217–220:77–95
10. Francfort G, Marigo J-J (1998) Revisiting brittle fracture as an energy minimization problem. J Mechanics Phys Solids 46:1319–1342
11. Wu J-Y et al (2020) Phase-field modeling of fracture. Adv Appl Mech 53:1–183
12. Chen P, Feng Y, Ma YE (2025) A high-accuracy phase field model for complex cohesive law. Eng Fracture Mech 315:110765
13. Feng Y, Hai L (2025) 3D phase-field cohesive fracture: unifying energy, driving force, and stress criteria for crack nucleation and propagation direction. J Mech Phys Solids 196:106036
14. Zhou X, Lu D, Zhang Y, Du X, Rabczuk T (2022) An open-source unconstrained stress updating algorithm for the modified Cam-clay model. Comput Methods Appl Mech Eng 390:114356
15. Nagaraja S *et al* (2019) Phase-field modeling of brittle fracture with multi-level hp-FEM and the finite cell method. *Computational Mechanics*
16. Ambati M, Gerasimov T, De Lorenzis L (2014) A review on phase-field models of brittle fracture and a new fast hybrid formulation. Comput Mech 55:383–405
17. Heister T, Wheeler MF, Wick T (2015) A primal-dual active set method and predictor-corrector mesh adaptivity for computing fracture propagation using a phase-field approach. Comput Methods Appl Mech Eng 290:466–495
18. Li S, Cui X (2020) N-sided polygonal smoothed finite element method (nsfem) with non-matching meshes and their applications for brittle fracture problems. Comput Methods Appl Mech Eng 359:112672
19. Xie K, Zhang R, Li Z, Wu Z (2023) Adaptive method for phase-field fracture using a volume weighted Quickselect algorithm. Int J Fracture 242:247–263
20. Tian F, Tang X, Xu T, Yang J, Li L (2019) A hybrid adaptive finite element phase-field method for quasi-static and dynamic brittle fracture. Int J Numerical Methods Eng 120:1108–1125
21. Zhang T, Hirshikesh YuT, Xing C, Natarajan S (2023) An adaptive dynamic phase-field method using the variable-node elements for cohesive dynamic fracture. Comput Methods Appl Mech Eng 416:116390
22. Hirshikesh Jansari C, Kannan K, Annabattula R, Natarajan S (2019) Adaptive phase field method for quasi-static brittle fracture using a recovery based error indicator and quadtree decomposition. Eng Fracture Mech 220:106599
23. Birk C, Pasupuleti AK, Assaf R, Natarajan S, Gravenkamp H (2024) On the use of scaled boundary shape functions in adaptive phase field modeling of brittle fracture. Comput Mech. https://doi.org/10.1007/s00466-024-02529-6
24. Goswami S, Anitescu C, Rabczuk T (2020) Adaptive fourth-order phase field analysis for brittle fracture. Comput Methods Appl Mech Eng 361:112808
25. Veiga L et al (2012) Basic principles of virtual element methods. Math Models Methods Appl Sci 23:199–214
26. Wriggers P, Aldakheel F (2024) Hudobivnik B virtual element methods in engineering sciences. Springer International Publishing, Berlin
27. Xu B-B, Fan W-L, Wriggers P (2024) High-order 3D virtual element method for linear and nonlinear elasticity. Comput Methods Appl Mech Eng 431:117258
28. Aldakheel F, Hudobivnik B, Hussein A, Wriggers P (2018) Phase-field modeling of brittle fracture using an efficient virtual element scheme. Comput Methods Appl Mech Eng 341:443–466
29. Liu T-R, Aldakheel F, Aliabadi M (2023) Virtual element method for phase field modeling of dynamic fracture. Comput Methods Appl Mech Eng 411:116050
30. Aldakheel F, Hudobivnik B, Wriggers P (2019) Virtual element formulation for phase-field modeling of ductile fracture. Int J Multiscale Comput Eng 17:181–200
31. Hudobivnik B, Aldakheel F (2022) Adaptive virtual element method for large-strain phase-field fracture. Springer, Berlin
32. Hussein A, Hudobivnik B, Wriggers P (2020) A combined adaptive phase field and discrete cutting method for the prediction of crack paths. Comput Methods Appl Mech Eng 372:113329
33. Leng Y *et al* (2024) Arbitrary order virtual element methods for high-order phase-field modeling of dynamic fracture. *Int J Numerical Methods Eng* **n/a**, e7605
34. Berrone S, Borio A, Marcon F, Teora G (2023) A first-order stabilization-free Virtual Element Method. Appl Math Lett 142:108641
35. Xu B-B, Peng F, Wriggers P (2023) Stabilization-free virtual element method for finite strain applications. Comput Methods Appl Mechanics Eng 417:116555
36. Xu B-B, Wriggers P (2024) 3D stabilization-free virtual element method for linear elastic analysis. Comput Methods Appl Mech Eng 421:116826
37. D'Altri A, Miranda S, Patruno L, Sacco E (2021) An enhanced VEM formulation for plane elasticity. Comput Methods Appl Mech Eng 376:113663
38. Xu B-B, Wang Y-F, Wriggers P (2024) Stabilization-free virtual element method for 2D elastoplastic problems. Int J Numerical Methods Eng 125:e7490
39. Berrone S, Borio A, Marcon F (2021) Lowest order stabilization free Virtual Element Method for the Poisson equation. *arXiv preprint:2103.16896*
40. van Huyssteen D, Lopez Rivarola F, Etse G, Steinmann P (2022) On mesh refinement procedures for the virtual element method for two-dimensional elastic problems. Comput Methods Appl Mech Eng 393:114849
41. van Huyssteen D, Lopez Rivarola F, Etse G, Steinmann P (2023) On adaptive mesh coarsening procedures for the virtual element method for two-dimensional elastic problems. Comput Methods Appl Mech Eng 418:116507
42. Winkler BJ (2001) *Traglastuntersuchungen von unbewehrten und bewehrten Betonstrukturen auf der Grundlage eines objektiven Werkstoffgesetzes fur Beton*. Ph.D. thesis, University of Innsbruck
43. Nguyen KD, Augarde EC, Coombs WM, Nguyen-Xuan H, Abdel-Wahab M (2020) Non-conforming multipatches for NURBS-based finite element analysis of higher-order phase-field models for brittle fracture. Eng Fracture Mech 235:107133